Available online at www.sciencedirect.com
ScienceDirect
Journal of Sound and Vibration 319 (2009) 335–354
JOURNAL OF SOUND AND VIBRATION
www.elsevier.com/locate/jsvi

Analysis of wave propagation in cylindrical pipes with local inhomogeneities

W.J. Zhou, M.N. Ichchou*, J.M. Mencik

Laboratoire de Tribologie et Dynamique des Systèmes, École Centrale de Lyon - 36, Avenue Guy de Collongues, 69130 Ecully, France

Received 16 October 2007; received in revised form 18 May 2008; accepted 26 May 2008
Handling Editor: A.V. Metrikine
Available online 14 July 2008

Abstract

In this paper, we present a numerical approach to study the guided elastic wave propagation in cylindrical pipes with local inhomogeneities. A hybrid wave finite element (WFE) and finite element (FE) technique is introduced to investigate the dispersion and wave scattering in pipes by taking full advantage of the existing FE codes. Dynamic reduction technique is employed to improve the computational efficiency, which is particularly suitable for the pipes with standard local features. Numerical examples indicate that the proposed technique provides an effective way to calculate the dispersion relationship and the scattered field. Both the axisymmetric and non-axisymmetric wave scattering problems are considered.

1. Introduction

Much of the existing literature focuses on the study of elastic guided waves and their practical applications in non-destructive testing (NDT) for long-range structures [1,2]. Unlike the classical ultrasound being used at local positions, those waves are tuned to have larger coverage ability from a single probe position by using pulse-echo method. Only a few measurements need to be performed through the remote inspection. Among those large-scale structures, pipes are used extensively in many important engineering industries; however, severe service conditions and environmental influence probably cause some damages and accelerate their aging progress. Many studies [3–12] are concentrated on the rapid inspection of pipes using the long-range evaluation technique, including the examination of interaction of the waves with defects or inclusions [3–7], the investigation of transducer technologies for wave generation [8–10], and the studies of phased array focusing in pipes [11,12]. The long-range inspection of pipes is essential especially when they are buried or partially unaccessible, since it is not practical to uncover the entire pipe for the inspection.

Guided waves with wavelengths several times larger than the pipe thickness are more attractive due to the lower attenuation [11]. As these waves travel along the pipes, they are particularly sensitive to transverse

*Corresponding author at: Equipe Dynamique des Systèmes et des Structures, Laboratoire de Mécanique des Solides, Génie Mécanique et Génie civil, 36 avenue Guy de collongue, BP 163, Ecole Centrale de Lyon, 69130 Ecully Cedex, France. Tel.: +33 4 72 18 62 30; fax: +33 4 72 18 91 44.
E-mail address: mohamed.ichchou@ec-lyon.fr (M.N. Ichchou).

0022-460X/$ - see front matter © 2008 Elsevier Ltd. All rights reserved.
doi:10.1016/j.jsv.2008.05.039

defects. However, the mechanism of the interaction between those waves and the defects or typical structural features should be investigated before conducting a rapid and effective quantitative evaluation of those pipes, which will contribute to the choice of frequency and modes for the localization or even sizing of different kinds of defects. Furthermore, if the excitation frequency is not well chosen, occurrence of local resonances at the joints or branch junctions where the energy propagation might be obstructed, will make the actual inspection distance much shorter than desired. Since the pipes can be made of anisotropic materials or multiple layers, analytical solution is possible but difficult to obtain [13]. Problems are further complicated if these waves interact with defects, and the geometrical features such as elbows and junctions, which are mostly irregular. Therefore numerical methods need to be resorted to assess the feasibility of guided wave inspections, among which the finite element (FE) method is most frequently used. Alleyne et al. [5] studied the reflection of axisymmetric longitudinal wave from the notches in pipes and the relationship between reflection ratio and the depths of notches. Demma et al. [6] presented a quantitative analysis for the reflection coefficient of guided waves from notches in pipes by using the standard FE method, where the three-dimensional (3-D) problem is considered. In fact, to deal with the problems in the view of wave propagation is more convenient than the conventional FE method which is used to analyse the bounded structures. Generally, the pipes are uniform in one direction so that the cross-section has the same physical and geometric properties. Such feature allows some semi-analytical or even analytical methods to be used. In the case that the pipe is partially inhomogeneous due to the occurrence of defects or structural features, the hybrid methods can be employed. Zhuang et al. [14] used a hybrid semi-analytical finite element (SAFE) method to investigate scattering of axisymmetric waves in a welded pipe containing a circumferential crack. Bai et al. [15] proposed a similar method to study wave scattering at transverse crack in the pipe, where the 3-D problem is considered; however, the method was developed only for the zero width planar cracks which is normal to the pipe axis. Similar methods are also implemented for plate waves. Galán and Abascal [16] used a hybrid SAFE/boundary element (BE) method to study Lamb wave scattering in semi-infinite plates. Zhao and Rose [17] used a hybrid analytical/BE method to investigate the scattering of both Lamb and horizontal shear (SH) waves in plates with surface break defects, where the normal modes come from the analytical solution.

In the present paper another numerical eigenmode extraction method is employed, which is based on the technique dealing with the wave propagation problems of periodic structures. Mead [18] proposed a general theory in order to determine harmonic wave propagation characters, where both one-dimensional (1-D) and two-dimensional (2-D) periodic systems are considered. Recently, more studies focus on extending this idea to homogenous structures rather than generally periodic systems comprised of an arbitrary substructure. This wave FE method regards the homogenous waveguide structure as a periodic system assembled by identical substructures [19]. Those substructures can be discretized with the aid of some commercial FE procedures, rather than the development of a relatively new FE code for specific elements. This allows the existing element libraries and powerful grid generation procedures to be used for many engineering structures. As the system matrices (usually available through the substructure or superelement analysis [20,21]) of a typical substructure is at hand before the eigenfunction need to be formed, the eigenfunction formulation is very different from that using SAFE method, though both methods lead to the quadratic eigenvalue problems with the same matrix size, if the equal number of nodes are used in the cross-section normal to the wave propagating axis. Houillon et al. [22] studied the wave propagation of homogenous thin-walled structures using this method. Duhamel et al. [23] used this method to investigate the vibrations of uniform waveguide structures, where it is proved to be accurate with relatively low computational cost in comparison with the standard FE method. Ichchou et al. [24] investigated the numerical sensitivity of this method. The method was also implemented for wave propagation and dynamic problems in the homogeneous structures with internal fluid [25–27], where the studies were based on the wave finite element (WFE) method for the 1-D wave propagation problem and concentrated on the lower frequency problems (far below the frequency of interest for NDT).

So far as the authors know, no previous studies have been published to extend this method to investigate the interaction of the elastic waves with the local inhomogeneities in the pipes, especially the higher frequency wave scattering problems which mostly concern relatively large FE models. In this work, we propose a hybrid WFE/FE method for the scattered field calculation, which is computationally expensive by using the full FE method if the frequency goes higher [6].

By using axisymmetric elements, WFE method for the 1-D wave propagation problem is employed to extract the wavenumbers and mode shapes for axisymmetric modes (longitudinal modes—$L(0, m)$ and torsional modes—$T(0, m)$, see the definition of the wave modes in Ref. [13] or Ref. [28]). Those eigenmodes are then superposed to form a scattering equation by connecting with FE formulation of the pipe segment with inhomogeneities.

In order to include more general local inhomogeneities than those considered by the aforementioned works, the dynamic reduction technique, component modal synthesis (CMS) is combined to formulate a numerically efficient scattering equation when dealing with the complex substructure models. This reduction technique fully takes into account the fact that the pipelines usually have some standard local features, and also allows various types of 3-D defects to be considered with ease.

As to the non-axisymmetric modes (flexural modes—$F(n, m)$), before connecting those eigenmodes to the dynamic reduced FE formulation, they are calculated by using the 3-D brick elements, which is based on the WFE formulation for the 2-D wave propagation problem [29]. Only the radial dimension is discretized. Consequently this treatment avoids the large-scale non-symmetric eigenvalue problems to be encountered during the frequently used 1-D wave propagation formulation for the whole pipe circle.

Numerical examples are given to illustrate the applicability of the presented formulation, with the results compared with standard FE results and some published experimental data. The proposed hybrid WFE/FE formulation is aimed at offering a convenient numerical scheme for the elastic wave scattering in the pipes with local defects and structural features, which principally involving the sensitivity analysis of specific elastic waves and the feasibility for their application of NDT in pipes.

2. Finite element analysis of axisymmetric waves

Since wave propagation properties in pipes are complex, it is necessary to study the axisymmetric mode properties with lower computational expense before treating with the 3-D problems. The axisymmetric guided waves in the hollow cylinders are similar to Lamb waves and SH waves in the plates. It is well known that their mode shapes converge as the radius to thickness ratio increases. They are a set of important waves including mostly popularly used $L(0, 2)$ and $T(0, 1)$ modes for pipe inspection [3–15].

2.1. Finite element description and dispersion relationship

For the 1-D wave propagation in the pipe, as is shown in Fig. 1, by utilizing the axisymmetric elements, the general FE formulation of a typical cell can be written as

$$\begin{bmatrix} \mathbf{D}_{ll} & \mathbf{D}_{li} & \mathbf{D}_{lr} \\ \mathbf{D}_{il} & \mathbf{D}_{ii} & \mathbf{D}_{ir} \\ \mathbf{D}_{rl} & \mathbf{D}_{ri} & \mathbf{D}_{rr} \end{bmatrix} \begin{Bmatrix} \mathbf{q}_l \\ \mathbf{q}_i \\ \mathbf{q}_r \end{Bmatrix} = \begin{Bmatrix} \mathbf{F}_l \\ \mathbf{F}_i \\ \mathbf{F}_r \end{Bmatrix}, \tag{1}$$

where $[\mathbf{D}]$ is the structured dynamic stiffness matrix, subscripts l, r and i denote the left, right and interior components, respectively. Assume that there exists no interior force ($\mathbf{F}_i = \mathbf{0}$); Eq. (1) can be simplified by

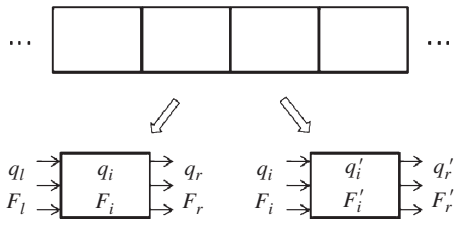

Fig. 1. Structure discretized to identical cells (one-dimensional periodic system).

eliminating the components of interior degree of freedoms (dofs) as

$$\begin{bmatrix} \mathbf{S}_{ll} & \mathbf{S}_{lr} \\ \mathbf{S}_{rl} & \mathbf{S}_{rr} \end{bmatrix} \begin{Bmatrix} \mathbf{q}_l \\ \mathbf{q}_r \end{Bmatrix} = \begin{Bmatrix} \mathbf{F}_l \\ \mathbf{F}_r \end{Bmatrix}, \tag{2}$$

where

$$\mathbf{S}_{ll} = \mathbf{D}_{ll} - \mathbf{D}_{li}\mathbf{D}_{ii}^{-1}\mathbf{D}_{il}, \quad \mathbf{S}_{lr} = \mathbf{D}_{lr} - \mathbf{D}_{li}\mathbf{D}_{ii}^{-1}\mathbf{D}_{ir},$$
$$\mathbf{S}_{rl} = \mathbf{D}_{rl} - \mathbf{D}_{ri}\mathbf{D}_{ii}^{-1}\mathbf{D}_{il}, \quad \mathbf{S}_{rr} = \mathbf{D}_{ri} - \mathbf{D}_{ri}\mathbf{D}_{ii}^{-1}\mathbf{D}_{ir}.$$

Therefore only the interface dofs are retained. Provided that there is no wave distortion induced by the material or geometric variation in the propagation direction, namely z-axis, the wave motions can be theoretically treated using the exponential function $e^{-ikz}(i = \sqrt{-1})$. Hence the displacement and force relationships between two adjacent cells are (see Fig. 1)

$$\mathbf{q}_l' = \mathbf{q}_l e^{-ikd}, \quad \mathbf{F}_l' = \mathbf{F}_l e^{-ikd}, \tag{3}$$

where d is the length of the cell in wave propagation direction. The time-dependent term $e^{i\omega t}$ is omitted here, and elsewhere for other expressions. Considering the displacement continuity $\mathbf{q}_l' = \mathbf{q}_r$ and force equilibrium condition $\mathbf{F}_l' = -\mathbf{F}_r$, Eq. (2) can be written as

$$\begin{bmatrix} \mathbf{S}_{ll} & \mathbf{S}_{lr} \\ \mathbf{S}_{rl} & \mathbf{S}_{rr} \end{bmatrix} \begin{Bmatrix} \mathbf{q}_l \\ \lambda\mathbf{q}_l \end{Bmatrix} = \begin{Bmatrix} \mathbf{F}_l \\ -\lambda\mathbf{F}_l \end{Bmatrix}, \tag{4}$$

where $\lambda = e^{-ikd}$ denotes the propagation constant. Eliminating the force component of Eq. (4) leads to a special case of quadratic eigenvalue problem for $(\lambda, \mathbf{q}_l)$

$$[\mathbf{S}_{rl} + \lambda(\mathbf{S}_{ll} + \mathbf{S}_{rr}) + \lambda^2\mathbf{S}_{rl}^{\mathrm{T}}]\mathbf{q}_l = 0, \tag{5}$$

where $\mathbf{S}_{rl}$, $\mathbf{S}_{ll}$ and $\mathbf{S}_{rr} \in \mathbb{C}^{N\times N}$, $\mathbf{S}_{ll}+\mathbf{S}_{rr} = (\mathbf{S}_{ll}+\mathbf{S}_{rr})^{\mathrm{T}}$. The eigenvalues of above eigenfunction Eq. (5) come in pairs $(\lambda, 1/\lambda)$, and if $\mathbf{q}_l$ is the right eigenvector of λ then $\mathbf{q}_l^{\mathrm{T}}$ is the left eigenvector of $1/\lambda$, which can be proved by taking the transpose of Eq. (5):

$$\mathbf{q}_l^{\mathrm{T}}[\mathbf{S}_{rl} + 1/\lambda(\mathbf{S}_{ll} + \mathbf{S}_{rr}) + 1/\lambda^2\mathbf{S}_{rl}^{\mathrm{T}}] = 0. \tag{6}$$

If the spectrum problem for both propagating and evanescent modes is of interest, the unknown propagation constant must be obtained for a given frequency in order to find the dispersion relationship. Reformulating Eq. (5) leads to

$$\begin{bmatrix} \mathbf{0} & \mathbf{S}_{rl} \\ -\mathbf{S}_{rl} & -\mathbf{S}_{ll} - \mathbf{S}_{rr} \end{bmatrix} \begin{Bmatrix} \mathbf{q}_l \\ \lambda\mathbf{q}_l \end{Bmatrix} = \lambda \begin{bmatrix} \mathbf{S}_{rl} & \mathbf{0} \\ \mathbf{0} & \mathbf{S}_{rl}^{\mathrm{T}} \end{bmatrix} \begin{Bmatrix} \mathbf{q}_l \\ \lambda\mathbf{q}_l \end{Bmatrix}. \tag{7}$$

The solution of such standard generalized eigenvalue problem yields the displacement vectors $\mathbf{q}_l^j$ $(j = 1, 2, \ldots, 2N)$ for propagating and non-propagating waves. The corresponding force vectors can be written as

$$\mathbf{F}_l^j = (\mathbf{S}_{ll} + \lambda^j\mathbf{S}_{lr})\mathbf{q}_l^j \tag{8}$$

which can be obtained from Eq. (4). However, the symmetry of the spectrum in Eq. (7) might be lost due to roundoff errors, if no preservation routine is used in the eigenvalue computation. In the case of large matrices produced, it is better to employ the structured linearization method proposed by Zhong and Williams [30], which calculates the reciprocal pairs $(\lambda, 1/\lambda)$ by constructing Eq. (5) to the eigenproblem about two skew symmetric matrices

$$\begin{bmatrix} \mathbf{S}_{rl} - \mathbf{S}_{rl}^{\mathrm{T}} & -(\mathbf{S}_{rr} + \mathbf{S}_{ll}) \\ (\mathbf{S}_{rr} + \mathbf{S}_{ll}) & \mathbf{S}_{rl} - \mathbf{S}_{rl}^{\mathrm{T}} \end{bmatrix} \begin{Bmatrix} \mathbf{q}_l \\ \lambda\mathbf{q}_l \end{Bmatrix} = \mu \begin{bmatrix} \mathbf{0} & \mathbf{S}_{rl} \\ -\mathbf{S}_{rl}^{\mathrm{T}} & \mathbf{0} \end{bmatrix} \begin{Bmatrix} \mathbf{q}_l \\ \lambda\mathbf{q}_l \end{Bmatrix}, \tag{9}$$

where $\mu = (1/\lambda + \lambda)$. The pairing of eigenvalues is automatically guaranteed, as the linearization itself preserves the symmetry. However, eigensolution of Eq. (9) need specific iteration procedure to be developed [30], so does the linearization method proposed in Ref. [31]. As the left system matrix is most likely well-conditioned,

Eq. (9) can be formulated as the standard eigenvalue problem:

$$[\mathbf{S}_{\mathrm{Std}}]\begin{Bmatrix}\mathbf{q}_l\\ \lambda\mathbf{q}_l\end{Bmatrix}=\frac{1}{\mu}\begin{Bmatrix}\mathbf{q}_l\\ \lambda\mathbf{q}_l\end{Bmatrix}, \tag{10}$$

where $[\mathbf{S}_{\mathrm{Std}}]$ equals to the left division of the right system matrix by the left one. The eigenvalues $1/\mu$ with the larger real parts correspond to the wavenumbers with the smaller amplitudes of imaginary parts, although not very strictly. This allows the ARPACK routine for non-symmetric complex eigenvalue problems to be used [32], which is faster than the QZ algorithm if only a few eigenpairs are of interest.

If the dispersion relation is available, the time-averaged axial energy flow in the pipe wall is $I=\frac{1}{T}\int_0^T \mathbf{F}^{\mathrm{H}}\dot{\mathbf{q}}\,\mathrm{d}t$, which written in Poynting vector is [18]

$$I_j=\langle P\rangle=\tfrac{1}{2}\mathrm{Re}\{\mathrm{i}\omega(\mathbf{F}_l^j)^{\mathrm{H}}\mathbf{q}_l^j\}, \tag{11}$$

where superscript H denotes Hermitian transpose.

The group velocity of a modulated wave is $V_g=\partial\omega/\partial k_R$, where k_R is the real part of the wavenumber. It equals to the energy velocity (or signal velocity) for the waves in undamped or slightly damped media. As to the waves in the highly absorptive media, it is well known that the group velocity cannot describe the manner that signal travels. The energy velocity is defined as the quotient of the time average energy flow and the energy density at the cross-section normal to the propagating axis [24],

$$V_e=\frac{\langle P\rangle}{\langle E\rangle}, \tag{12}$$

where $E=T+U$, which stands for the sum of potential and kinetic energy density at the cross-section. Considering that the typical cell with length d, expression Eq. (12) for energy velocity can be defined at the mid cross-section, where

$$\langle P_{\mathrm{mid}}\rangle=\frac{1}{2}\mathrm{e}^{k_I d}\mathrm{Re}\{\mathrm{i}\omega\mathbf{F}_l^{\mathrm{H}}\mathbf{q}_l\}, \tag{13}$$

where k_I is the imaginary part of the wavenumber. The average kinetic and potential energy density at the mid cross-section is approximated as

$$\langle T\rangle=\frac{1}{4d}\omega^2\mathbf{q}_{lr}^{\mathrm{H}}\mathbf{M}\mathbf{q}_{lr},\quad \langle U\rangle=\frac{1}{4d}\mathbf{q}_{lr}^{\mathrm{H}}\mathbf{K}\mathbf{q}_{lr}, \tag{14}$$

where $\mathbf{q}_{lr}=(\mathbf{q}_l^{\mathrm{T}},\mathbf{q}_r^{\mathrm{T}})^{\mathrm{T}}$, $\mathbf{M}$ and $\mathbf{K}$ are the mass and stiffness matrices condensed on the left and right boundaries. Thus, expression Eq. (12) for energy velocity becomes

$$V_e=\frac{2d\,\mathrm{e}^{k_I d}\mathrm{Re}\{\mathrm{i}\omega\mathbf{F}_l^{\mathrm{H}}\mathbf{q}_l\}}{\mathbf{q}_{lr}^{\mathrm{H}}(\mathbf{K}+\omega^2\mathbf{M})\mathbf{q}_{lr}}. \tag{15}$$

It should be mentioned that if the dispersion relationships in undamped systems are of interest, Eq. (5) can be re-formed to the generalized eigenvalue problem for ω^2 about two Hermitian matrices, which provides a rapid dispersion calculation scheme.

2.2. Scattering equation and its dynamic reduction form

Consider an infinitely long pipe with the local inhomogeneities which are due to the geometry or material variation. A monochromatic incident wave, which comprises a single or multiple wave modes, is assumed to be generated at $z-\infty$ and travel in the positive $z+\infty$ direction. Scattering phenomenon emerges when the incident wave impinges on those inhomogeneities, as is shown in Fig. 2 schematically. The resultant wave field consists of the incident and scattered components (both reflection and transmission).

2.2.1. Mode expansion and scattering equation formula

To describe the scattered field, eigensolution need to be decomposed to positive- and negative-going wave modes for the computational purpose. If the hysteretic damping is introduced by complex stiffness,

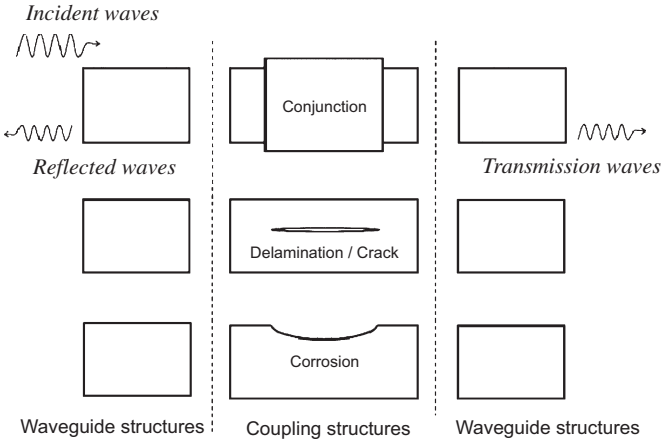

Fig. 2. Waves scattering at local defects and junction.

eigensolution of Eq. (7) or Eq. (9) will not yield the real or purely imaginary wavenumbers. Then the eigen modes ($\mathbf{q}^j$, $\mathbf{F}^j$), where $j = 1, 2, \ldots, 2N$, can be divided into two sets with the same number: ($[\mathbf{q}^-]$, $[\mathbf{F}^-]$) with $|\lambda| < 1$ representing negative-going waves, ($[\mathbf{q}^+]$, $[\mathbf{F}^+]$) with $|\lambda| > 1$ representing positive-going waves, which are written as N by N base matrices. For the undamped system, there exists the case $|\lambda| = 1$ relating to the purely propagating waves, which can also be decomposed to positive-going and negative-going waves by observing the sign of the imaginary part of λ.

As the mode bases are split, the incident, reflected and transmission waves can be expanded as the superposition of the whole mode bases. In fact, not all the bases should be taken into account, although they are generally linear independent. This is mainly due to the fact that the higher order evanescent modes only occur at the immediate vicinity of the inhomogeneities, since the non-reflecting boundaries are considered in this study. In addition, the FE discretization with limited number of elements cannot predict those eigenmodes and the corresponding field vectors within acceptable precision. Furthermore, the base reduction allows some available procedures been used [32], and also makes the scattered field calculation computationally cost effective.

By using the reduced bases with base number N_r ($N_r < N$), the incident, reflected and transmission waves can be expressed as

$$\mathbf{q}^{\mathrm{inc}} = [\mathbf{q}^+]\mathbf{\Lambda}^+\mathbf{A}^{\mathrm{inc}}, \quad \mathbf{q}^{\mathrm{ref}} = [\mathbf{q}^-]\mathbf{\Lambda}^-\mathbf{A}^{\mathrm{ref}}, \quad \mathbf{q}^{\mathrm{tra}} = [\mathbf{q}^+]\mathbf{\Lambda}^+\mathbf{A}^{\mathrm{tra}}, \tag{16}$$

where $\mathbf{q}^{\mathrm{inc}}$ and $\mathbf{q}^{\mathrm{tra}}$ are formed of the same bases, $[\mathbf{q}^+]$ and $[\mathbf{q}^-]$ are normalized N by N_r matrices, $\mathbf{A}^{\mathrm{inc}}$, $\mathbf{A}^{\mathrm{ref}}$, and $\mathbf{A}^{\mathrm{tra}}$ denote the amplitudes of the corresponding waves, $\mathbf{\Lambda}^+$ and $\mathbf{\Lambda}^-$ are diagonal matrices relating respectively to the positive- and negative-going waves, which are given as

$$\mathbf{\Lambda}^{\pm} = \mathrm{diag}\{\mathrm{e}^{\mp \mathrm{i}k_j z}\}, \quad (j = 1, 2, \ldots, N_r). \tag{17}$$

Since the relationship between displacement vectors and force vectors Eq. (8) holds, the expressions of $\mathbf{F}^{\mathrm{inc}}$, $\mathbf{F}^{\mathrm{ref}}$ and $\mathbf{F}^{\mathrm{tra}}$ are analogous:

$$\mathbf{F}^{\mathrm{inc}} = [\mathbf{F}^+]\mathbf{\Lambda}^+\mathbf{A}^{\mathrm{inc}}, \quad \mathbf{F}^{\mathrm{ref}} = [\mathbf{F}^-]\mathbf{\Lambda}^-\mathbf{A}^{\mathrm{ref}}, \quad \mathbf{F}^{\mathrm{tra}} = [\mathbf{F}^+]\mathbf{\Lambda}^+\mathbf{A}^{\mathrm{tra}}, \tag{18}$$

where

$$[\mathbf{F}^{\pm}] = \mathbf{S}_{ll}[\mathbf{q}^{\pm}] + \mathbf{S}_{lr}[\mathbf{q}^{\pm}]\mathrm{diag}\{\mathrm{e}^{\mp \mathrm{i}k_j d}\}. \tag{19}$$

When those waves are connected with the inhomogeneous part, the interface can be established adjacent to the excitation resource or the discontinuities in order to satisfy the coupling conditions. As the truncated modal bases are used, they may not be sufficient to satisfy a "continuous" but probably arbitrary stress function, if the interface is set to be very close to the inhomogeneities. Consequently, the coupling structure

model sometimes need to cover a part of waveguide structures to avoid the high order evanescent waves being predicted at the interface, as is shown in Fig. 2. The extension size depends on the frequency of interest and the irregularities of the coupling structures in contrast to the waveguide features. Thus the truncated bases, which consist of all the propagating modes and a set of evanescent modes, will allow the displacement and stress field to be represented by an expansion over those modes.

The modelling of damaged cell is similar to that of typical one for modes extraction, except that additional interior dofs might be included. The coupling condition is governed by the dynamics equation of coupling structures,

$$[\mathbf{M}^c]\left\{ (\ddot{\mathbf{q}}_l^c)^{\mathrm{T}} \quad (\ddot{\mathbf{q}}_i^c)^{\mathrm{T}} \quad (\ddot{\mathbf{q}}_r^c)^{\mathrm{T}} \right\}^{\mathrm{T}} + [\mathbf{K}^c]\left\{ (\mathbf{q}_l^c)^{\mathrm{T}} \quad (\mathbf{q}_i^c)^{\mathrm{T}} \quad (\mathbf{q}_r^c)^{\mathrm{T}} \right\}^{\mathrm{T}} = \left\{ (\mathbf{F}_l^c)^{\mathrm{T}} \quad \mathbf{0} \quad (\mathbf{F}_r^c)^{\mathrm{T}} \right\}^{\mathrm{T}}, \tag{20}$$

where $[\mathbf{M}^c]$ and $[\mathbf{K}^c]$ denote the mass and stiffness matrices of coupling structures, respectively. Eq. (20) can be condensed as

$$\begin{bmatrix} \mathbf{S}_{ll}^c & \mathbf{S}_{lr}^c \\ \mathbf{S}_{rl}^c & \mathbf{S}_{rr}^c \end{bmatrix} \begin{Bmatrix} \mathbf{q}_l^c \\ \mathbf{q}_r^c \end{Bmatrix} = \begin{Bmatrix} \mathbf{F}_l^c \\ \mathbf{F}_r^c \end{Bmatrix}. \tag{21}$$

Considering the coupling conditions

$$\mathbf{q}_l^c = [\mathbf{q}^+]\mathbf{A}^{\mathrm{inc}} + [\mathbf{q}^-]\mathbf{A}^{\mathrm{ref}}, \quad \mathbf{q}_r^c = [\mathbf{q}^+]\mathbf{A}^{\mathrm{tra}} \tag{22}$$

and

$$\mathbf{F}_l^c = [\mathbf{F}^+]\mathbf{A}^{\mathrm{inc}} + [\mathbf{F}^-]\mathbf{A}^{\mathrm{ref}}, \quad \mathbf{F}_r^c = -[\mathbf{F}^+]\mathbf{A}^{\mathrm{tra}}. \tag{23}$$

Eq. (21) can be re-formed as the governing equations for the scattering problem:

$$\begin{bmatrix} \mathbf{S}_{ll}^c[\mathbf{q}^-] - [\mathbf{F}^-] & \mathbf{S}_{lr}^c[\mathbf{q}^+] \\ \mathbf{S}_{rl}^c[\mathbf{q}^-] & \mathbf{S}_{rr}^c[\mathbf{q}^+] + [\mathbf{F}^+] \end{bmatrix} \begin{Bmatrix} \mathbf{A}^{\mathrm{ref}} \\ \mathbf{A}^{\mathrm{tra}} \end{Bmatrix} = \begin{bmatrix} [\mathbf{F}^+] - \mathbf{S}_{ll}^c[\mathbf{q}^+] \\ -\mathbf{S}_{rl}^c[\mathbf{q}^+] \end{bmatrix} \{\mathbf{A}^{\mathrm{inc}}\}. \tag{24}$$

Given a single or a set of incident modes as the input in Eq. (24), scattered modes (reflection and transmission) acting as the output can be obtained. Numerically, the base number N_r is suggested to be frequency dependent, which can be implemented by a routine to include those slightly evanescent wave modes into the bases.

2.2.2. *Dynamic reduction for coupling structure modelling*

Local defects or complex structural features most likely induce a coupling structure model with large dofs since higher grid density is required. The FE grid might be locally refined in order to well characterize the models. On the other hand, higher order evanescent modes play an important role when the scattering arises from a severe discontinuity. They are more likely excited as the frequency goes higher. Whereas the modes extraction procedure will be time-consuming if those modes need to be predicted precisely, the further enlarged coupling structure is required to avoid their emergence at the interface. The computational burden is then suggested to switch to the modelling of the coupling structures. However, the system matrices of coupling parts at each frequency in Eq. (21) have to be taken into calculation. In this case, a convenient way is to model the coupling structure using component mode synthesis (CMS) method, which gives better approximation than Guyan reduction (exact for stiffness matrices but approximate for mass) when dealing with higher frequency problems.

For the sake of simplicity, the fixed-boundary CMS method is used here [33]. In the fixed-boundary CMS method, a substructure is considered to be composed of interior and interface dofs. It condenses the system matrices by assuming the displacements of the interior dofs as a linear superposition of the constraint modes and the internal normal modes. Introduce the transformation matrix $[\mathbf{T}]$, the displacement vector of coupling substructure is represented in terms of generalized coordinates:

$$\left\{ (\mathbf{q}_l^c)^{\mathrm{T}} \quad (\mathbf{q}_i^c)^{\mathrm{T}} \quad (\mathbf{q}_r^c)^{\mathrm{T}} \right\}^{\mathrm{T}} = [\mathbf{T}]\left\{ (\mathbf{q}_l^c)^{\mathrm{T}} \quad (\mathbf{q}_\delta^c)^{\mathrm{T}} \quad (\mathbf{q}_r^c)^{\mathrm{T}} \right\}^{\mathrm{T}}, \tag{25}$$

where the $\mathbf{q}_\delta^c$ is the modal displacement. The transformation matrix for the fixed-boundary method has the form

$$[\mathbf{T}] = \begin{bmatrix} \mathbf{I} & \mathbf{0} & \mathbf{0} \\ -[\mathbf{K}_{ii}^c]^{-1}[\mathbf{K}_{il}^c] & \mathbf{\Phi}_{ii} & -[\mathbf{K}_{ii}^c]^{-1}[\mathbf{K}_{ir}^c] \\ \mathbf{0} & \mathbf{0} & \mathbf{I} \end{bmatrix}, \tag{26}$$

where $\mathbf{\Phi}_{ii}$ is the fixed interface normalized modal matrix, $\mathbf{K}_{ii}^c$, $\mathbf{K}_{il}^c$ and $\mathbf{K}_{ir}^c$ are the interior dofs related components in the stiffness matrix. Thus Eq. (20) can be simplified as

$$[\mathbf{M}_{CB}^c]\left\{ (\ddot{\mathbf{q}}_l^c)^{\mathrm{T}} \quad (\ddot{\mathbf{q}}_\delta^c)^{\mathrm{T}} \quad (\ddot{\mathbf{q}}_r^c)^{\mathrm{T}} \right\}^{\mathrm{T}} + [\mathbf{K}_{CB}^c]\left\{ (\mathbf{q}_l^c)^{\mathrm{T}} \quad (\mathbf{q}_\delta^c)^{\mathrm{T}} \quad (\mathbf{q}_r^c)^{\mathrm{T}} \right\}^{\mathrm{T}} = \left\{ (\mathbf{F}_l^c)^{\mathrm{T}} \quad \mathbf{0} \quad (\mathbf{F}_r^c)^{\mathrm{T}} \right\}^{\mathrm{T}}, \tag{27}$$

where the condensed mass matrix $[\mathbf{M}_{CB}^c] = [\mathbf{T}]^{\mathrm{T}}[\mathbf{M}^c][\mathbf{T}]$, stiffness matrix $[\mathbf{K}_{CB}^c] = [\mathbf{T}]^{\mathrm{T}}[\mathbf{K}^c][\mathbf{T}]$, $\mathbf{q}_\delta$ is the truncated set of generalized modal displacement associated to the modal matrix $\mathbf{\Phi}_{ii}$.

Consequently, Eq. (24) can be modified as

$$\begin{bmatrix} \hat{\mathbf{S}}_{ll}^c[\mathbf{q}^-] - [\mathbf{F}^-] & \hat{\mathbf{S}}_{lr}^c[\mathbf{q}^+] \\ \hat{\mathbf{S}}_{rl}^c[\mathbf{q}^-] & \hat{\mathbf{S}}_{rr}^c[\mathbf{q}^+] + [\mathbf{F}^+] \end{bmatrix} \begin{Bmatrix} \mathbf{A}^{\mathrm{ref}} \\ \mathbf{A}^{\mathrm{tra}} \end{Bmatrix} = \begin{bmatrix} [\mathbf{F}^+] - \hat{\mathbf{S}}_{ll}^c[\mathbf{q}^+] \\ -\hat{\mathbf{S}}_{rl}^c[\mathbf{q}^+] \end{bmatrix} \{\mathbf{A}^{\mathrm{inc}}\}, \tag{28}$$

where $\hat{\mathbf{S}}_{ll}^c$, $\hat{\mathbf{S}}_{lr}^c$, $\hat{\mathbf{S}}_{rl}^c$, $\hat{\mathbf{S}}_{rr}^c$ are the reduced system matrices obtained by eliminating the modal displacement $\mathbf{q}_\delta$. After solving Eq. (28), the whole scattered wave fields can be obtained through Eqs. (25)–(27) for near field and the wave representation (Eqs. (16) and (18)) for far field. It should be noted that the eigensolution of the coupling substructure model can be used for different wave inputs, which is particularly applicable to the systems comprising certain standard local features. Another advantage over the direct condensation is that the number of the normal modes of coupling substructures can also be frequency dependent, not only that of the truncated bases, which further improves the numerical efficiency if the solution in the wide frequency range is desired.

3. Finite element analysis of non-axisymmetric waves

There are another set of modes which can propagate in the cylindrical pipes. These modes have integer circumferential wavenumbers. As been investigated in the previous section, the properties of the axisymmetric modes and their interaction with axisymmetric defects can be conveniently investigated since there is no variation of displacements and stresses field around the circumference. However, practical defects are mostly irregular and non-axisymmetric. When the incident axisymmetric waves impinge on those irregular defects, the modes will lose some energy being converted to the non-axisymmetric modes, causing the complex 3-D scattering problems. In addition, it is not easy to have purely axisymmetric modes generated even by the aid of some advanced excitation schemes [13].

The application of WFE method for the 1-D wave propagation analysis of non-axisymmetric waves is not as effortless as that for the plate waves or axisymmetric cylindrical waves, because it generally requires more computation resources owing to the introduce of the circumferential waves numbers, especially when the diameter is relatively large. It is necessary to treat the harmonic variation of the mode structures theoretically in both the circumferential and axial directions, i.e. using $\lambda_a = \mathrm{e}^{-\mathrm{i}kd}$ to denote the axial wave propagating constant, while $\lambda_c = \mathrm{e}^{-\mathrm{i}n\Delta\theta}$ ($n \in \mathbb{Z}$) the circumferential propagating constant. This treatment is similar to that for the 2-D periodic systems considered by Ahmed in Ref. [29], where the high order elements were used. In this study, the cell is assumed to be discretized by the linear shell or brick elements without interior dofs for the case of clarity (see Fig. 3). Let the circumferential wavenumber n be non-negative integer, i.e. we firstly consider the axisymmetric modes and positive circumferential wave. The dynamic equation for the typical 3-D cell of the pipe is

$$[\mathbf{D}_{ij}]\{\mathbf{q}_{l1} \quad \mathbf{q}_{l2} \quad \mathbf{q}_{r1} \quad \mathbf{q}_{r2}\}^{\mathrm{T}} = \{\mathbf{F}_{l1} \quad \mathbf{F}_{l2} \quad \mathbf{F}_{r1} \quad \mathbf{F}_{r2}\}^{\mathrm{T}}, \tag{29}$$

where $[\mathbf{D}_{ij}]$ ($i,j = 1, 2, 3, 4$) is the structured dynamic stiffness matrix of the typical cell in cylindrical coordinate system. Considering the periodicity conditions for the mode structures, the relationship of the displacement

$$\mathbf{q}_{l2} = \lambda_c \mathbf{q}_{l1}, \quad \mathbf{q}_{r1} = \lambda_a \mathbf{q}_{l1}, \quad \mathbf{q}_{r2} = \lambda_a \lambda_c \mathbf{q}_{l1}, \tag{30}$$

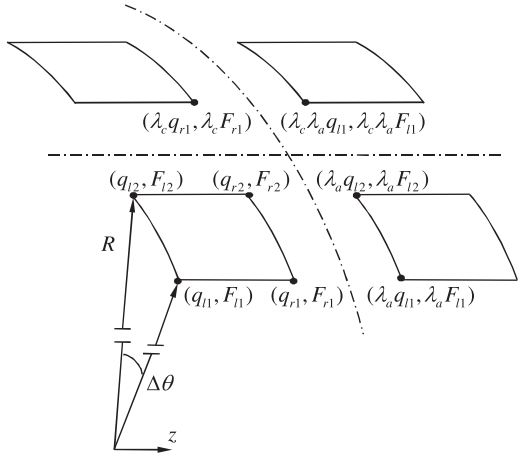

Fig. 3. Three-dimensional pipe model built in cylindrical coordinate space with the cells assembled as two-dimensional periodic system.

and the force equilibrium condition

$$\mathbf{F}_{r2} = -(\lambda_a\lambda_c\mathbf{F}_{l1} + \lambda_a\mathbf{F}_{l2} + \lambda_c\mathbf{F}_{r1}) \tag{31}$$

holds, as is schematically indicated in Fig. 3. Then Eq. (29) can be reduced to form the eigenfunction

$$(\lambda_a^2\mathbf{S}_1 + \lambda_a\mathbf{S}_2 + \mathbf{S}_3)\mathbf{q}_{l1} = 0, \tag{32}$$

where $\mathbf{S}_1 = \lambda_c^2\mathbf{D}_{14} + \lambda_c(\mathbf{D}_{13} + \mathbf{D}_{24}) + \mathbf{D}_{23}$, $\mathbf{S}_2 = \lambda_c^2(\mathbf{D}_{12} + \mathbf{D}_{34}) + \lambda_c(\mathbf{D}_{11} + \mathbf{D}_{22} + \mathbf{D}_{33} + \mathbf{D}_{44}) + \mathbf{D}_{21} + \mathbf{D}_{43}$, $\mathbf{S}_3 = \lambda_c^2\mathbf{D}_{32} + \lambda_c(\mathbf{D}_{31} + \mathbf{D}_{42}) + \mathbf{D}_{41}$.

It can be proved that the eigenvalues of above eigenfunction Eq. (32) come in pairs $(\lambda_a, 1/\lambda_a)$, because λ_c is direction independent due to the symmetry (it can be set to be $e^{in\Delta\theta}$), if λ_a is regarded as eigenvalue, and vice versa. Strict proof need the properties of the block matrices to be considered.

Similar to the eigenfunction in the axisymmetric cases, Eq. (32) can be linearized as

$$\begin{bmatrix} \mathbf{S}_1 - \mathbf{S}_3 & -\mathbf{S}_2 \\ \mathbf{S}_2 & \mathbf{S}_1 - \mathbf{S}_3 \end{bmatrix} \begin{Bmatrix} \mathbf{q}_{l1} \\ \lambda_a\mathbf{q}_{l1} \end{Bmatrix} = \mu \begin{bmatrix} \mathbf{0} & \mathbf{S}_1 \\ -\mathbf{S}_3 & \mathbf{0} \end{bmatrix} \begin{Bmatrix} \mathbf{q}_{l1} \\ \lambda_a\mathbf{q}_{l1} \end{Bmatrix}, \tag{33}$$

where $\mu = \lambda_a + 1/\lambda_a$, or simply as

$$\begin{bmatrix} \mathbf{0} & \mathbf{I} \\ -\mathbf{S}_3 & -\mathbf{S}_2 \end{bmatrix} \begin{Bmatrix} \mathbf{q}_{l1} \\ \lambda_a\mathbf{q}_{l1} \end{Bmatrix} = \lambda_a \begin{bmatrix} \mathbf{I} & \mathbf{0} \\ \mathbf{0} & \mathbf{S}_1 \end{bmatrix} \begin{Bmatrix} \mathbf{q}_{l1} \\ \lambda_a\mathbf{q}_{l1} \end{Bmatrix}, \tag{34}$$

if a smaller model is of interest.

The wavenumbers and mode structures for both propagating and evanescent waves are available by solving Eq. (33) or Eq. (34) for a given circumferential wavenumber in frequency domain. Although they concern the quadratic eigenvalue problems, the computational cost is nearly negligible, as only the radial dimension of the pipe need to be discretized. Similar to Eq. (5), Eq. (32) can also be constructed as the eigenfunction with smaller system matrices for the circular frequency if only the dispersion curves are desired.

In order to connect with the FE formulation of the coupling structures, the displacement and force vectors should be extracted from the eigensolution. Let $(\mathbf{q}_l, \mathbf{F}_l)$, $(\mathbf{q}_r, \mathbf{F}_r)$ denote the left and right vectors respectively. By reusing the periodicity conditions, the left displacement vector can be written as

$$\mathbf{q}_l = \left(\mathbf{q}_{l1}^{\mathrm{T}}, \lambda_c\mathbf{q}_{l1}^{\mathrm{T}}, \ldots, \lambda_c^{m-1}\mathbf{q}_{l1}^{\mathrm{T}}, \ldots, \lambda_c^{M-1}\mathbf{q}_{l1}^{\mathrm{T}}\right)^{\mathrm{T}}, \tag{35}$$

where $M = 2\pi/\Delta\theta$, $m = 1,2,\ldots, M$. Analogously, the right displacement vector is

$$\mathbf{q}_r = \left(\mathbf{q}_{r1}^{\mathrm{T}}, \lambda_c\mathbf{q}_{r1}^{\mathrm{T}}, \ldots, \lambda_c^{m-1}\mathbf{q}_{r1}^{\mathrm{T}}, \ldots, \lambda_c^{M-1}\mathbf{q}_{r1}^{\mathrm{T}}\right)^{\mathrm{T}}, \tag{36}$$

or written as $\mathbf{q}_r = \lambda_a \mathbf{q}_l$ due to the relationship given by Eq. (30). The left force vector can be formed as

$$\mathbf{F}_l = \left(\mathbf{F}_{l1}^{\mathrm{T}} + \lambda_c^{M-1}\mathbf{F}_{l2}^{\mathrm{T}}, \ldots, \lambda_c^{m-1}\mathbf{F}_{l1}^{\mathrm{T}} + \lambda_c^{m-2}\mathbf{F}_{l2}^{\mathrm{T}}, \ldots, \lambda_c^{M-1}\mathbf{F}_{l1}^{\mathrm{T}} + \lambda_c^{M-2}\mathbf{F}_{l2}^{\mathrm{T}}\right)^{\mathrm{T}}. \tag{37}$$

And the right vector is

$$\mathbf{F}_r = \left(\mathbf{F}_{r1}^{\mathrm{T}} + \lambda_c^{M-1}\mathbf{F}_{r2}^{\mathrm{T}}, \ldots, \lambda_c^{m-1}\mathbf{F}_{r1}^{\mathrm{T}} + \lambda_c^{m-2}\mathbf{F}_{r2}^{\mathrm{T}}, \ldots, \lambda_c^{M-1}\mathbf{F}_{r1}^{\mathrm{T}} + \lambda_c^{M-2}\mathbf{F}_{r2}^{\mathrm{T}}\right)^{\mathrm{T}}, \tag{38}$$

or written as $\mathbf{F}_r = -\lambda_a \mathbf{F}_l$ since the relationship given by Eq. (31) holds.

As n is supposed to be non-negative, solution of Eq. (32) leads to waves which are circumferentially propagating (or non-propagating), rather than the modes like those obtained in the axisymmetric cases. Another solution is also necessary by setting the circumferential constant $\lambda_c^{\theta-} = -\mathrm{e}^{\mathrm{i}n\Delta\theta}$. The bases for non-axisymmetric waves are then duplicated. The non-axisymmetric modes in pipes with infinite length can be described as the linear combination of the positive circumferential ($\theta+$) waves and negative circumferential ($\theta-$) waves from two solutions:

$$\mathbf{q} = (a\mathbf{q}_{l1}^{\theta+}\mathrm{e}^{-\mathrm{i}n\theta} + b\mathbf{q}_{l1}^{\theta-}\mathrm{e}^{\mathrm{i}n\theta})\mathrm{e}^{-\mathrm{i}kz}, \quad \mathbf{F} = (a\mathbf{F}_{l1}^{\theta+}\mathrm{e}^{-\mathrm{i}n\theta} + b\mathbf{F}_{l1}^{\theta-}\mathrm{e}^{\mathrm{i}n\theta})\mathrm{e}^{-\mathrm{i}kz}. \tag{39}$$

Thus all the circumferentially standing or propagating modes can be predicted. The scattering formulation can be constructed by resorting to Eq. (24) or its dynamic reduction form (Eq. (28)), which can be utilized to deal with wave scattering at any type of local inhomogeneities.

4. Numerical results and discussion

4.1. Axisymmetric waves and the interaction with axisymmetric inhomogeneities

4.1.1. Convergence analysis and dispersion calculation

A convergence analysis considering different grid densities through the thickness is performed in order to determine the proper modelling size within the frequency range of interest. Without loss of generality, the pipes are assumed to be isotropic and single layered, so it is easier to validate the numerical procedures by the analytical solution for cylindrical Lamb or torsional waves.

In order to compare to the numerical and experimental studies in Ref. [3], a steel pipe is considered, with the material properties and geometry being set as: density $\rho = 7850\,\mathrm{kg/m^3}$, Young's modulus $E = 2.169 \times 10^{11}\,\mathrm{Pa}$, Poisson's ratio $v = 0.287$, internal diameter $\phi_{\mathrm{ID}} = 76\,\mathrm{mm}$, wall thickness $h = 5.5\,\mathrm{mm}$. The linear quadrilateral axisymmetric element with eight dofs is used to study the axisymmetric waves. The dispersion curves calculated with different grid densities is shown in Fig. 4(a). It suggests that the though-thickness

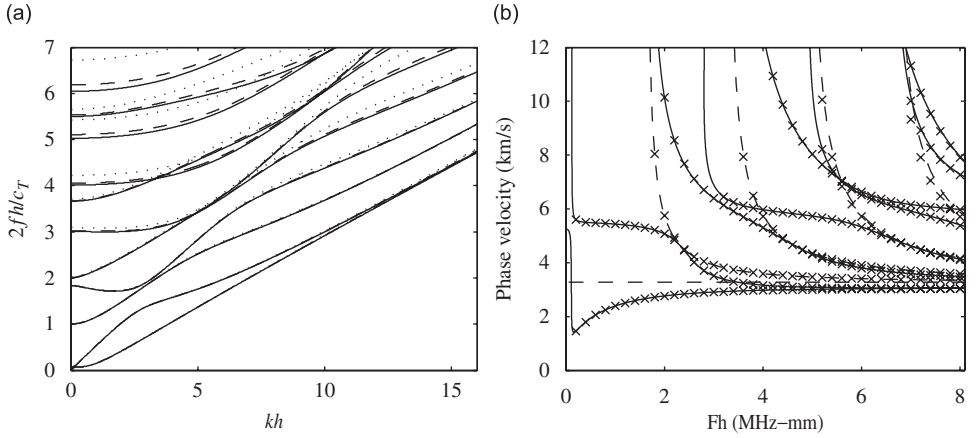

Fig. 4. Convergence analysis and validation of dispersion relationship. (a) dispersion curves of axisymmetric Lamb modes for 76 mm (ID) steel pipe with different grid densities: (——) 45 nodes, (– –) 23 nodes, ($\cdots$) 12 nodes; (b) phase velocity dispersion of axisymmetric modes for 76 mm (ID) steel pipe: (——) $L(0,m)$ modes by FE with 23 nodes, (– –) $T(0,\mathrm{m})$ modes by FE with 23 nodes, ($\times\ \times$) analytical.

discretization by 22 linear elements will provide sufficient accuracy for the modes with the thickness frequency production below 8 MHz mm. At 8 MHz mm, the error of the wavenumbers for the propagating modes are smaller than 0.8%. Introduce the grid criterion proposed in Ref. [16] for the plate modes calculation using SAFE method,

$$N_c = \frac{\lambda_T}{L} > \beta, \tag{40}$$

where N_c is the number of elements per through-thickness "wavelength", L is the element size, $\lambda_T = 2\pi c_T/\omega$ is the transverse "wavelength", $\beta = 10$ is suggested for linear elements and $\beta = 4$ for quadratic elements. At 8 MHz mm N_c equals to 9. If employ the quadratic elements with the same number of nodes, it is faster to approach the convergence due to the quadratic interpolation, which is also indicated in that paper. This means the criterion is also applicable to some extent in this case. As to the torsional modes, the linear quadrilateral elements with each having four dofs are used. Fig. 4(b) gives a comparison of the analytical and FE results for the phase velocity dispersion. The analytical method is implemented by the root searching procedure for a given frequency [13]. Agreements are found before the higher order modes appear. The group velocity dispersion curves below 6 MHz mm are shown in Fig. 5(a). If the high dissipation is considered and introduced as the structural damping with loss factor $\eta = 0.05$, the energy velocity prediction calculated using Eq. (15) is given in Fig. 5(b), where group velocity curves are provided for comparison. It can be seen that they fit well only in the region where the attenuation is low. Significant divergence is observed in high attenuation region, especially near the cut-off frequency for undamped case in Fig. 5(a).

4.1.2. Interaction with surface breaking defects

For the scattering problems of L(0, m) modes, the mesh density is kept unchanged, while the upper frequency is reduced to 6 MHz mm, where $N_c = 12$. This consideration is driven by the better prediction for a set of non-propagating modes, which are to be included into the truncated bases. For instance, at 4.4 MHz mm the bases comprise five propagating modes ($L(0,1)$–$L(0,5)$) and five non-propagating modes ($L(0,5)$–$L(0,10)$), whose mode structures are partially shown in Fig. 6. At least six elements per transverse wavelength are ensured for those non-propagating modes.

Schematically shown in Fig. 7, half elliptical notches with $l = h/5$ and the through-thickness extension h_d/h varying from 5% to 95% are considered to model the flawed pipe. Fig. 8 shows the reflection and transmission coefficient of different notch depths, which are calculated by the dynamic reduced scattering equation with sufficient fixed modes considered to approach the convergence. Fig. 9 shows a comparison of results calculated with different number of fixed modes included in the dynamic reduced scattering equation. It indicates that agreements of two methods will be achieved within the frequency band of $[0, f_{\max}]$ by taking account of the fixed modes below $1.2f_{\max}$.

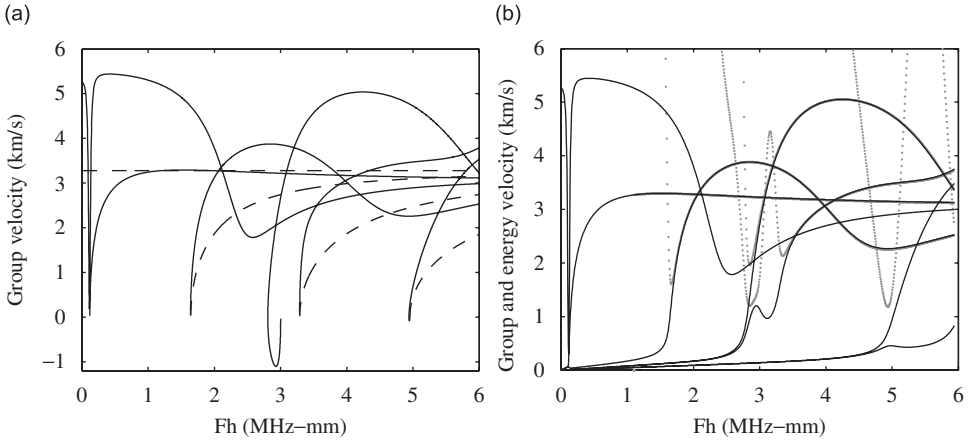

Fig. 5. Group and energy velocity. (a) group velocity dispersion of axisymmetric modes: (——) $L(0, 1)$–$L(0, 6)$, (– –) $T(0, 1)$–$T(0, 4)$; (b) comparison of group velocity V_g ($\cdots$) and energy velocity V_e (——) ($\eta = 0.05$).

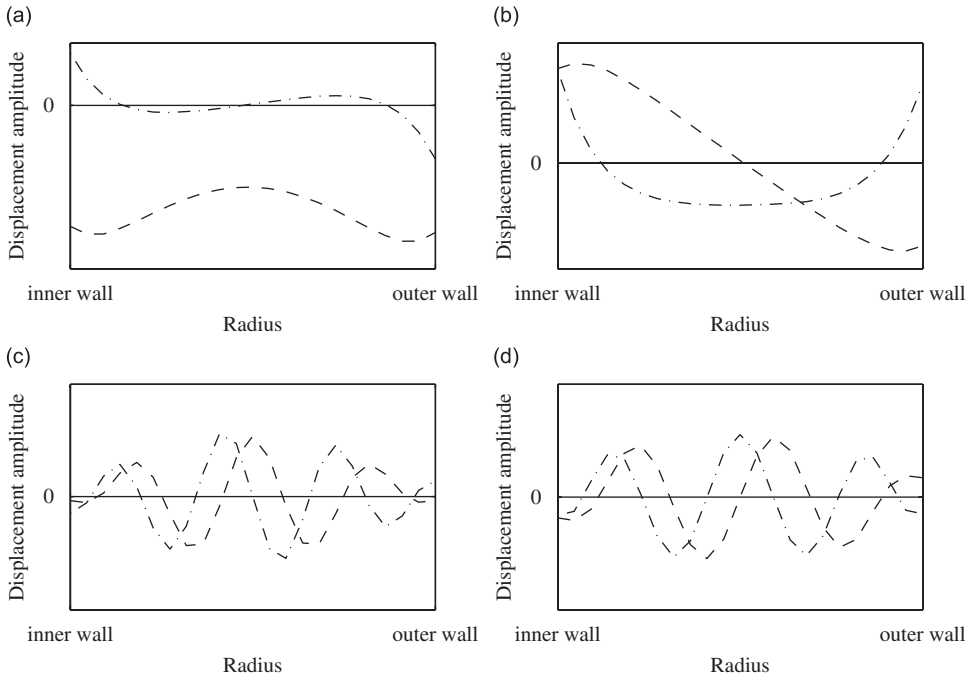

Fig. 6. Mode structures at 4.4 MHz mm. (a)—L (0, 1), (b)—L (0, 2), (c)—L (0, 9), (d)—L (0, 10), (––) radial displacement, (– ·) axial displacement.

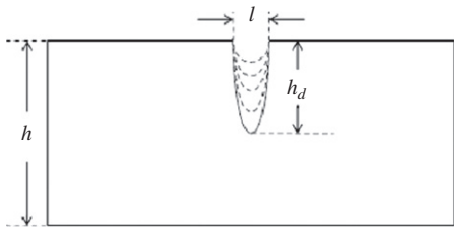

Fig. 7. Modelling elliptical defects with the depth 10%, 20%, …, 50% of pipe thickness.

In order to validate the results obtained, a time domain analysis is performed through the standard FE calculation (implicit, explicit or Fourier transform based) of a bounded pipe model. The reflection and transmission coefficient can be calculated by dividing the Fourier spectrum of the reflected and transmitted signal by that of the incident signal. A 2.6 m long steel pipe with a notch 1.69 m away from the initial end is considered. To minimize the effect of defect induced dispersion, narrow band signals are used, typically composed of 5.5 cycles modulated by a Hanning window with the central frequency equal to 70 kHz. The axial displacements are monitored between the excitation end and the notch for the incident and reflected signal, as is shown in Fig. 10. Because those wave packets are apparently unconnected in this case, no wave packet decomposition techniques are needed. The frequency-dependent coefficients can be obtained by

$$|R(\omega)| = \frac{|\mathscr{F}(u_R(t))|}{|\mathscr{F}(u_I(t))|}\, e^{-k_I(\omega)L_1}, \quad |T(\omega)| = \frac{|\mathscr{F}(u_T(t))|}{|\mathscr{F}(u_I(t))|}\, e^{-k_I(\omega)L_2}, \tag{41}$$

where $u_R(t)$ and $u_I(t)$ denote the reflection and incident wave packet signal, respectively; L_1 and L_2 represent the distance between the notch and two corresponding monitoring spots. Fig. 11(a) shows the reflection coefficient evolution of different notch depths in frequency domain. It can be seen that the deviation of two

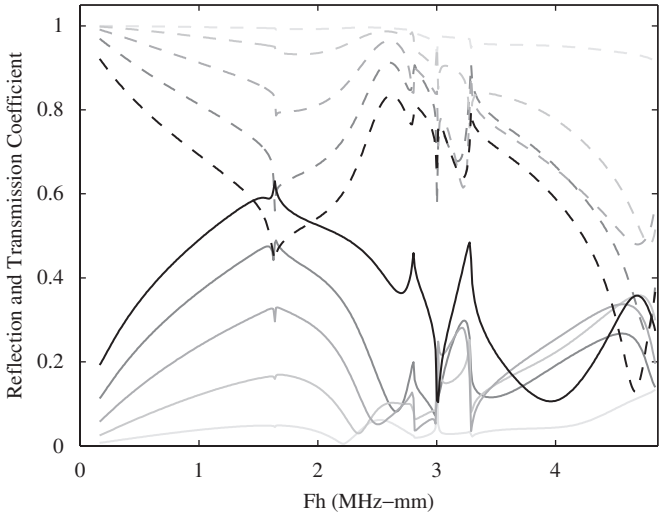

Fig. 8. Reflection $|R_{L(0,2)}|$ (—) and transmission $|T_{L(0,2)}|$ (– –) coefficient evolution with the notch depth variation from 10% to 50% (varying with the grey level increasing).

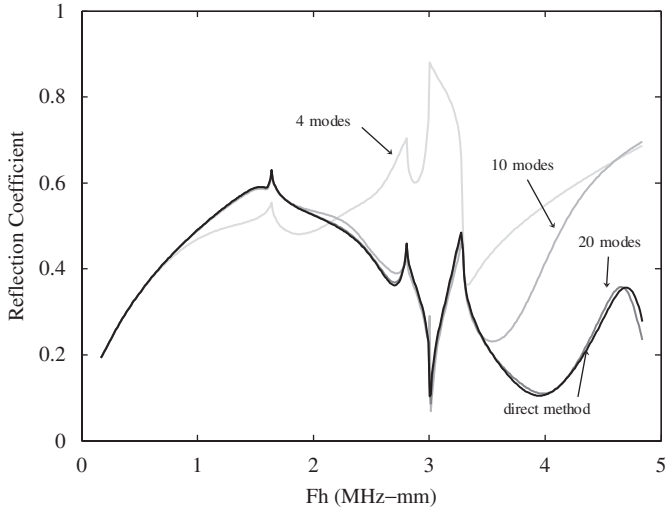

Fig. 9. Reflection $|R_{L(0,2)}|$ with different number of fixed modes included.

results are restricted within 5% in amplitude, so do those results at 70 kHz in Fig. 11(b), where the experimental data given in Ref. [5] is superposed for comparison, which suggests the similar tendency within acceptable discrepancies. The time domain analysis generally underestimate the reflection coefficient. This is probably because the grid in the analysis was limited by computational resource, consequently not refined enough, which made the flawed part "stiffer" than that used in scattering equation.

The scattering of $T(0, 1)$ modes are also analysed using 50 linear quadrilateral elements. Sharp notches with $l = h/10$ are firstly considered. Fig. 12 shows the reflection and transmission coefficient evolution with various notch depths in a wider frequency band, where the convergence of both the eigenmodes and the scattered mode distributions at upper frequency corresponding to different grid densities is checked. With the change of the notch depth, monotonic variations in the amplitude of reflection and transmission coefficient are observed. Those coefficients do not change much at the higher frequencies. In the case of the notch width increasing, the

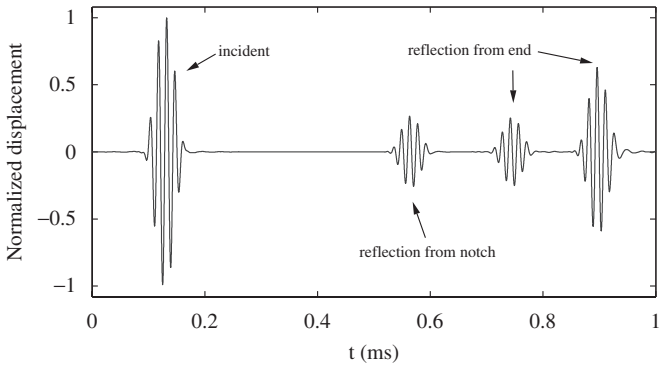

Fig. 10. Time response from FE calculation.

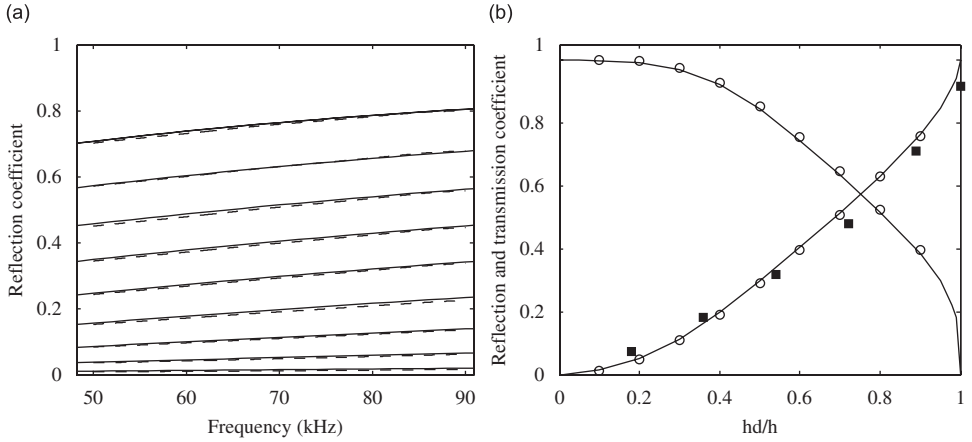

Fig. 11. Comparison with time domain analysis and experiment results in Ref. [5]. (a) reflection coefficient ($L(0, 2)$ at 50–90 kHz) variation with the notch depth: (——) WFE prediction, (– –) time-domain results; (b) reflection and transmission coefficient ($L(0, 2)$ at 70 kHz) variation with the notch depth: (——) WFE prediction, (○ ○) time-domain results, (■ ■) experiment results [5].

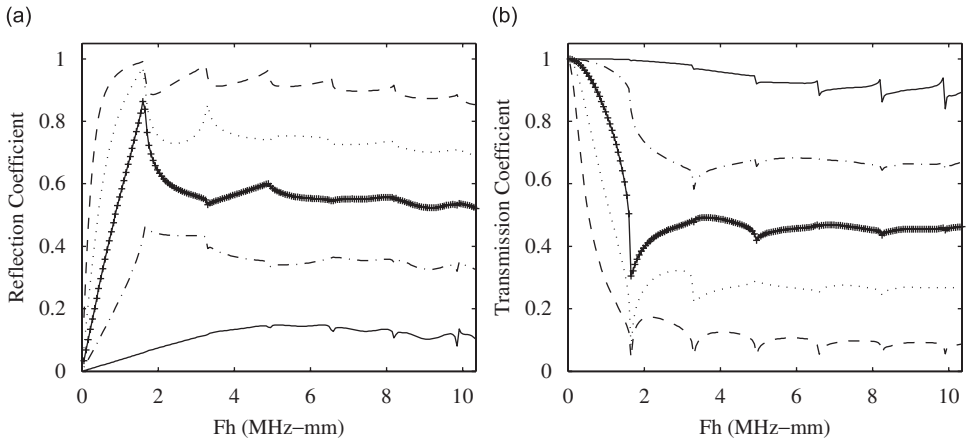

Fig. 12. Reflection ($|R_{T(0,1)}|$) and transmission ($|T_{T(0,1)}|$) coefficient variation with the notch depth: (—) 10%, (– ·) 30%, (+ +) 50%, (···) 70%, and (– –) 90%. (a) $|R_{T(0,1)}|$, (b) $|T_{T(0,1)}|$.

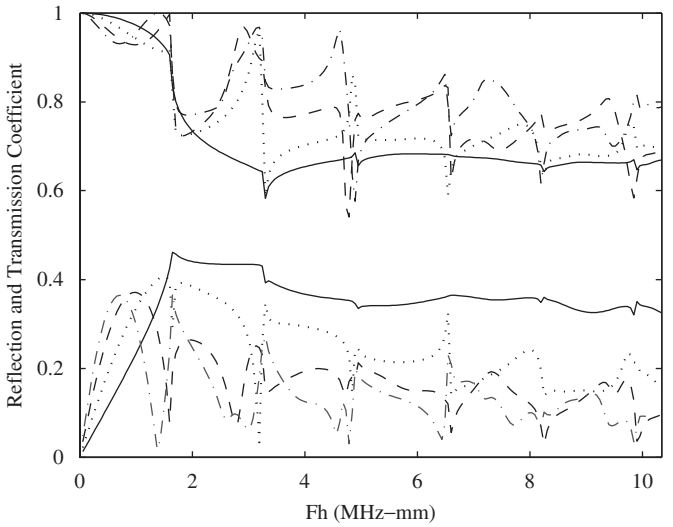

Fig. 13. Reflection ($|R_{T(0,1)}|$) and transmission coefficient ($|T_{T(0,1)}|$) variation with the notch length/depth ratio ($h_d/h = 0.3$): (—) $l/h_d = 0.5$, (···) $l/h_d = 1$, (– –) $l/h_d = 2$, and (– ·) $l/h_d = 4$.

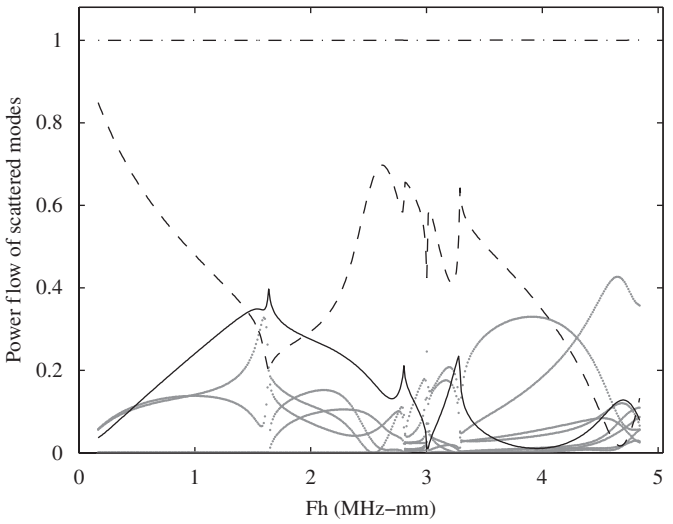

Fig. 14. Power flow of scattered modes (notch depth 50% of the thickness): (—) reflection of $L(0, 2)$, (– –) transmission $L(0, 2)$, (···) other scattered modes, and (– ·) summation of all the scattered modes.

coefficients tend to evolve severely with the frequency (see Fig. 13). This is because the local "resonances" further complicate the energy distribution among multiple modes, as the notch width turn to be comparable to the wavelength. Similar results are found in Ref. [17], where the reflection and transmission coefficients of the SH0 wave scattering in the flawed plates are given.

To further verify the numerical procedures, the energy conservation in terms of incident and scattered power flow equivalence is examined. The summation of power flows of all the scattered modes, which are normalized to that of the incident mode, should be unity over the entire frequency band, provided that no dissipation mechanisms are introduced. For the two cases shown in Figs. 14 and 15, the power flow summations vary within the interval 1 ± 10^{-5} and 1 ± 10^{-6}, respectively, which suggests that sufficient accuracy is achieved.

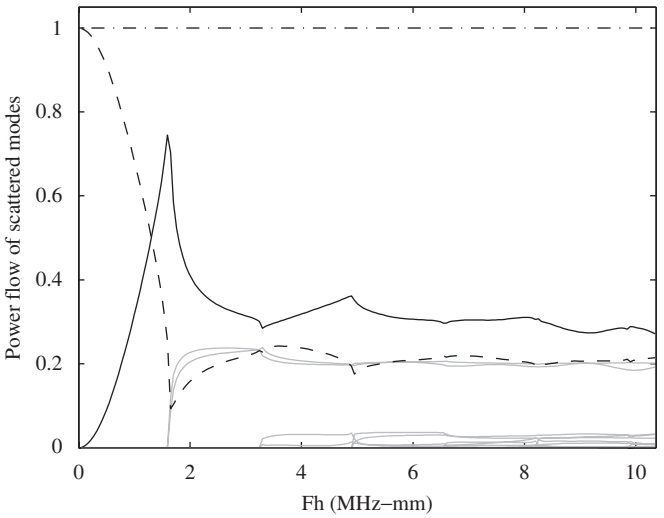

Fig. 15. Power flow of scattered modes (notch depth 50% of the thickness): (—) reflection of $T(0,1)$, (– –) transmission $T(0,1)$, (⋯) other scattered modes, and (– ·) summation of all the scattered modes.

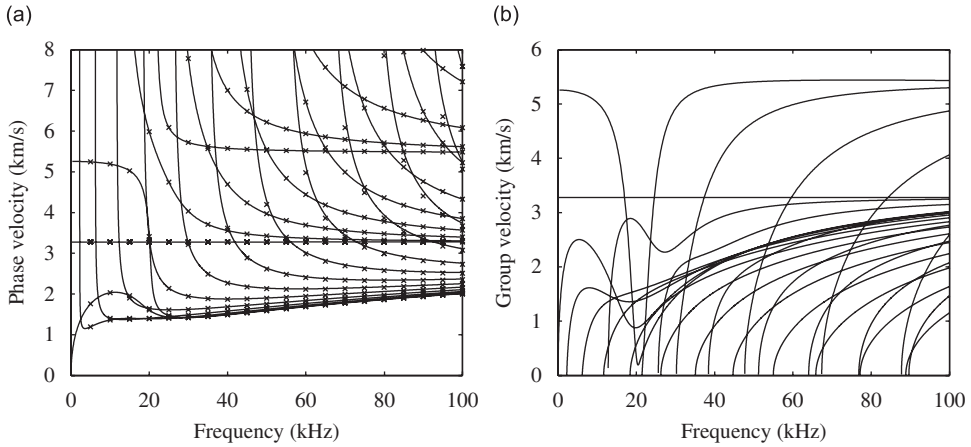

Fig. 16. Phase and group velocity dispersion for 76 mm (ID) steel pipe. (a) phase velocity, (——) WFE with 4 linear elements, (× ×) analytical; (b) group velocity (WFE with 4 linear elements).

4.2. Wave scattering at non-axisymmetric inhomogeneities

A 3-D cell consisted of four linear brick elements is used to extract the dispersion relationship below 100 kHz, as is given in Fig. 16. Here the dynamic stiffness matrices relating to Cartesian coordinate system from the standard FE packages are transformed to those relating to cylindrical coordinates (u_r,u_θ,u_z). For the linear brick elements, the dynamic stiffness matrix $\mathbf{D}$ relative to the dofs of a single node and its corresponding node at 2θ are transformed to $\mathbf{D}' = \mathbf{T}_c^{\mathrm{T}}\mathbf{D}\mathbf{T}_c$, where $\mathbf{T}_c = \mathrm{diag}\{\mathbf{P},\ 1,\ -\mathbf{P}^{\mathrm{T}},\ 1\}$ with $\mathbf{P} = (\sin\theta,\ -\cos\theta;\ \cos\theta,\ \sin\theta)$. The analytical results of phase velocity are also provided in Fig. 16, which are in agreement with those from WFE method, since more than 10 elements per wavelength in WFE calculation is sufficient to ensure the accuracy.

Through-thickness notches with axial extension equal to 2.5 mm and the circumferential extension varying from 10% to 90% are considered to examine the interaction of $L(0,\ 2)$ mode with non-axisymmetric inhomogeneities. The coupling structures are discretized into approximately 4000 brick elements with the

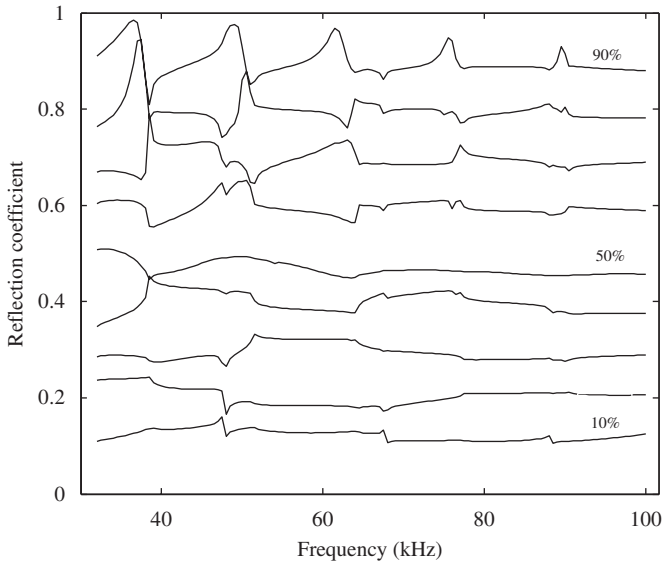

Fig. 17. Reflection coefficient $|R_{L(0,2)}|$ evolution with the notch extension varying from 10% to 90% of the pipe circumference.

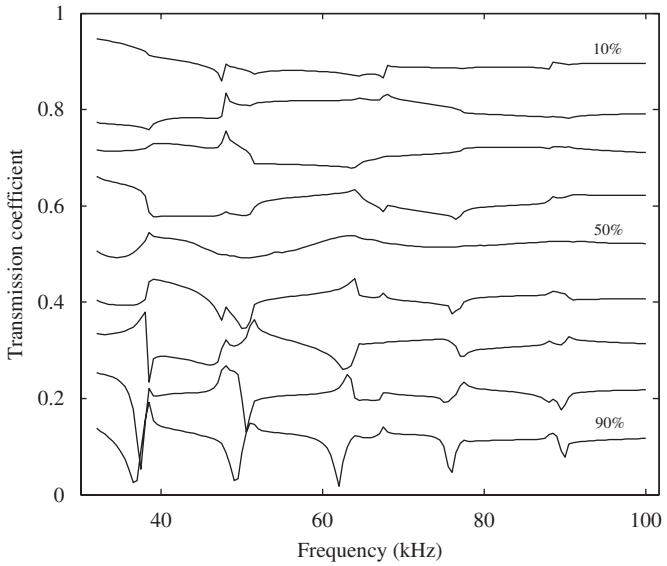

Fig. 18. Transmission coefficient $|T_{L(0,2)}|$ evolution with the notch extension varying from 10% to 90% of the pipe circumference.

cross-section having 384 elements to well characterize the notch features. As a wide frequency band is considered, the number of the modes that are included to the bases for the scattering problem is set to be frequency dependent. For an instance, 39 bases for the propagating modes (three symmetric and 18 non-symmetric modes) and a doubled number of bases for the non-propagating modes are chosen to form the truncated bases for positive-going modes at the frequency of 80 kHz. Figs. 17 and 18 show the reflection and transmission coefficient of $L(0, 2)$ mode, respectively, where monotonic changes of the coefficients are observed. These coefficients are not highly sensitive to the frequency within a wide band, except near to the cut-off frequency of $F(n, 3)$ modes, which is due to the close mode structures as the incident $L(0, 2)$ mode.

Fig. 19 gives the coefficients of scattered modes with the notch circumferential extension equal to 50% of the pipe circle. The mode conversions are extremely complex because a severe notch is considered, thus the

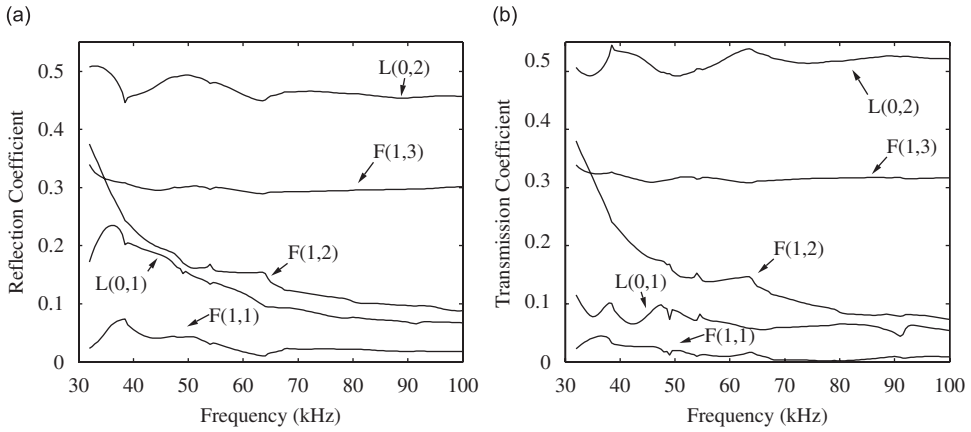

Fig. 19. Reflection and transmission coefficient of scattered modes with the notch extension 50% of the pipe circumference.

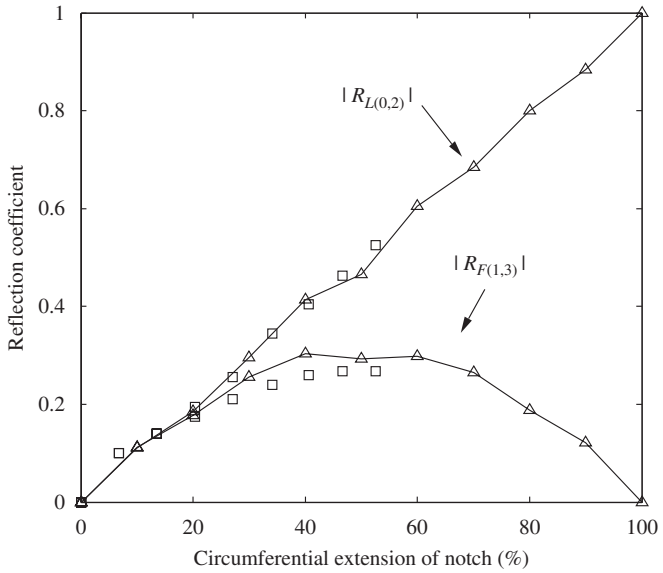

Fig. 20. Reflection coefficient of $L(0, 2)$ and converted mode $F(1, 3)$ at 70 kHz with different circumferential notch extensions: (–△–) WFE-FE calculation, and (□ □) experiment results in Ref. [3].

coefficients of only a few scattered modes are shown, besides the mostly converted $F(1, 3)$ mode. In fact, most of the scattered modes are predicted, except the $T(0,1)$ mode and some over included evanescent modes. This suggests that a sufficient number of modes should be considered when dealing with general non-axisymmetric inhomogeneities. However, in the case that the local inhomogeneities do not seriously destroy the axisymmetry, such as surface corrosion in steel pipe, the modes with large circumferential wavenumbers can be discarded, though they may be even propagating. This treatment will save the computational time while achieve acceptable numerical accuracy.

Fig. 20 gives the reflection coefficient of $L(0, 2)$ and converted mode $F(1, 3)$ at 70 kHz with various circumferential notch extensions. Experiment results from Ref. [3] are superposed for comparison. Both results exhibit the similar tendency of the reflection coefficient varieties. The coefficient of $F(1, 3)$ from numerical calculation is larger than that provided in Ref. [3]. This is probably caused by the fact that more severe notches are considered in the numerical studies than the experiments.

5. Conclusion

This paper investigates the elastic wave scattering at local inhomogeneities in pipes by utilizing a hybrid WFE/FE formulation. Numerical studies are given for both the axisymmetric and non-axisymmetric problems, which are partially validated by time domain analysis and the published experiment results. Numerical results show that the proposed formulation provides a convenient and effective way to calculate the wave modes and the scattered field. One of the advantages of the WFE method is that the waveguide model can be discretized by the aid of existing FE packages including powerful grid generation procedures to cope with wave propagation or dynamic problems of complex waveguide structures. It can be conveniently combined with FE method to analyse the wave scattering at local defects or structural features. Comparing to other methods such as SAFE method, the application of this method can be totally examined based on some existing FE packages, including the typical cell modelling, eigenfunction solution and substructure analysis.

The scattering of the lower frequency wave at non-axisymmetric pipe discontinuities is considered based on a 2-D formulation. If the frequency goes higher hence the wavelength is much smaller than the discontinuities, the circular scattered waves might appear. To correctly describe the scattered field, more eigenmodes need to be included to the mode expansion bases. The scattering field calculation for such 3-D scattering problems will be difficult even when the dynamic reduction technique being used.

Acknowledgement

The authors are grateful to the financial support from Elyo Ltd.

References

[1] J.L. Rose, M.J. Avioli, P. Mudge, et al., Guided wave inspection potential of defects in rail, *NDT&E International* 37 (2004) 153–161.
[2] J.L. Rose, Ultrasonic guided waves in structural health monitoring, *Key Engineering Materials* 270–273 (2004) 14–21.
[3] M.J.S. Lowe, D.N. Alleyne, P. Cawley, Defect detection in pipes using guided waves, *Ultrasonics* 36 (1998) 147–154.
[4] A. Demma, P. Cawley, M. Lowe, The reflection of the fundamental torsional mode from cracks and notches in pipes, *Journal of the Acoustical Society of America* 114 (2003) 611–625.
[5] D.N. Alleyne, M.J.S. Lowe, P. Cawley, The reflection of guided waves from circumferential notches in pipes, *Journal of Applied Mechanics* 65 (1998) 635–641.
[6] A. Demma, P. Cawley, M.J.S. Lowe, et al., The reflection of guided waves from notches in pipes: a guide for interpreting corrosion measurements, *NDT&E International* 37 (2004) 167–180.
[7] J. Ma, F. Simonetti, M.J.S. Lowe, Scattering of the fundamental torsional mode by an axisymmetric layer inside a pipe, *Journal of the Acoustical Society of America* 120 (2006) 1871–1880.
[8] D. Guo, T. Kundu, A new transducer holder mechanism for pipe inspection, *Journal of the Acoustical Society of America* 110 (1) (2001) 303–309.
[9] W.B. Na, T. Kundu, Underwater pipe inspection using guided waves, *ASME Journal of Pressure Vessel Technology* 124 (2) (2002) 196–200.
[10] W.B. Na, T. Kundu, EMAT-based inspection of concrete filled steel pipes for internal voids and inclusions, *ASME Journal of Pressure Vessel Technology* 124 (2002) 265–272.
[11] J. Barshinger, J.L. Rose, M.J. Avioli Jr., Guided wave resonance tuning for pipe inspection, *Journal of Pressure Vessel Technology* 124 (2002) 303–310.
[12] Wei Luo, Joseph L. Rose, Phased array focusing with guided waves in a viscoelastic coated hollow cylinder, *Journal of the Acoustical Society of America* 121 (4) (2007) 1945–1955.
[13] J.L. Rose, *Ultrasonic Waves in Solid Media*, Cambridge University Press, New York, NY, 1999.
[14] W. Zhuang, A.H. Shah, S.K. Datta, Axisymmetric guided wave scattering by cracks in welded steel pipes, *ASME, Journal Pressure Vessel Technology* 119 (1997) 401–406.
[15] H. Bai, A.H. Shah, N. Popplewell, S.K. Datta, Scattering of guided Waves by circumferential cracks in steel pipes, *ASME, Journal of Applied Mechanics* 68 (2001) 619–631.
[16] J.M. Galán, R. Abascal, Numerical simulation of Lamb wave scattering in semi-infinite plates, *International Journal for Numerical Methods in Engineering* 53 (2002) 1145–1173.
[17] X.G. Zhao, J.L. Rose, Boundary element modeling for defect characterization potential in a wave guide, *International Journal of Solids and Structures* 40 (2003) 2645–2658.
[18] D.J. Mead, A general theory of harmonic wave propagation in linear periodic systems with multiple coupling, *Journal of Sound and Vibration* 27 (1973) 235–260.

[19] B.R. Mace, D. Duhamel, M.J. Brennan, L. Hinke, Finite element prediction of wave motion in structural waveguides, *Journal of the Acoustical Society of America* 117 (2005) 2835–2843.
[20] NASTRAN, *MSC/NASTRAN—Advanced Dynamic Analysis Users Guide Version 70*, MSC Software Corp., Santa Ana, CA, USA, 2002.
[21] ANSYS, Inc. *Theory reference*. ANSYS release 9.0, 2004.
[22] L. Houillon, M.N. Ichchou, L. Jezequel, Wave motion in thin-walled structures, *Journal of Sound and Vibration* 281 (2005) 483–507.
[23] D. Duhamel, B.R. Mace, M.J. Brennan, Finite element analysis of the vibrations of waveguides and periodic structures, *Journal of Sound and Vibration* 294 (2006) 205–220.
[24] M.N. Ichchou, S. Akrout, J.-M. Mencik, Guided waves group and energy velocities via finite elements, *Journal of Sound and Vibration* 305 (2007) 931–944.
[25] A. Bocquillet, M.N. Ichchou, L. Jezequel, Energetics of axisymmetric fluid-filled pipes up to high frequencies, *Journal of Fluids and Structures* 17 (2003) 491–510.
[26] M. Maess, N. Wagner, L. Gaul, Dispersion curves of fluid filled elastic pipes by standard FE models and eigenpath analysis, *Journal of Sound and Vibration* 296 (2006) 264–276.
[27] J.-M. Mencik, M.N. Ichchou, Wave finite elements in guided elastodynamics with internal fluid, *International Journal of Solids and Structures* 44 (2007) 2148–2167.
[28] M.G. Silk, K.F. Bainton, The propagation in metal tubing of ultrasonic wave modes equivalent to Lamb waves, *Ultrasonics* 17 (1) (1979).
[29] Y.A.A. Ahmed, Matrix Analysis of Wave Propagation in Periodic Systems, Ph.D. Thesis, University of Southampton, 1979.
[30] W.X. Zhong, F.W. Williams, On the direct solution of wave propagation for repetitive structures, *Journal of Sound and Vibration* 181 (1995) 485–501.
[31] D.S. Mackey, N. Mackey, C. Mehl, V. Mehrmann, Structured polynomial eigenvalue problems: good vibrations from good linearizations, *SIAM Journal on Matrix Analysis and Applications* 28 (2006) 1029.
[32] R.B. Lehoucq, D.C. Sorensen, C. Yang, *ARPACK Users' Guide: Solution of Large-Scale Eigenvalue Problems with Implicitly Restarted Arnoldi Methods*, SIAM Publications, Philadelphia, 1998.
[33] R.R. Craig, M.D.D. Bampton, Coupling of substructures for dynamic analysis, *AIAA Journal* 12 (1968) 1313–1319.